



Cite this: *Nanoscale*, 2021, **13**, 6764

Received 12th November 2020,

Accepted 19th February 2021

DOI: 10.1039/d0nr08097g

rsc.li/nanoscale

Highly catalytically active CeO_{2-x}-based hetero-junction nanostructures with mixed micro/mesoporous architectures†

Sajjad S. Mofarah,^a Luisa Schreck,^a Claudio Cazorla,^b Xiaoran Zheng,^a Esmail Adabifiroozjaei,^{c,d} Constantine Tsounis,^e Jason Scott,^e Reza Shahmiri,^a Yin Yao,^f Roozbeh Abbasi,^g Yuan Wang,^{h,i} Hamidreza Arandiyani,^{i,j} Leigh Sheppard,^k Vienna Wong,^a Esmail Doustkhah,^l Pramod Koshy^a and Charles C. Sorrell^{*a}

The architectural design of nanocatalysts plays a critical role in the achievement of high densities of active sites but current technologies are hindered by process complexity and limited scalability. The present work introduces a rapid, flexible, and template-free method to synthesize three-dimensional (3D), mesoporous, CeO_{2-x} nanostructures comprised of extremely thin holey two-dimensional (2D) nanosheets of centimetre-scale. The process leverages the controlled conversion of stacked nanosheets of a newly developed Ce-based coordination polymer into a range of stable oxide morphologies controllably differentiated by the oxidation kinetics. The resultant polycrystalline, hybrid, 2D–3D CeO_{2-x} exhibits high densities of defects and surface area as high as 251 m² g⁻¹, which yield an outstanding CO conversion performance (T_{90%} = 148 °C) for all oxides. Modification by the creation of heterojunction nanostructures using transition metal oxides

(TMOs) results in further improvements in performance (T_{90%} = 88 °C), which are interpreted in terms of the active sites associated with the TMOs that are identified through structural analyses and density functional theory (DFT) simulations. This unparalleled catalytic performance for CO conversion is possible through the ultra-high surface areas, defect densities, and pore volumes. This technology offers the capacity to establish efficient pathways to engineer nanostructures of advanced functionalities for catalysis.

Introduction

Three dimensional (3D) mesoporous metal oxides (MOs) hold great promise in catalysis through increasing accessibility of the active sites relative to bulk materials. Nonetheless, the use of sacrificial templates, which generally are employed to introduce the pores and allow the formation of the 3D structures, makes the fabrication process complex and of low efficiency. Certain shortcomings also apply to various etching techniques for creating pores in 3D scaffolds.^{1,2} In porous structures, the walls of the 3D scaffolds limit the number of active sites to only the surface and subsurface of these 3D units.⁴⁷ The recently developed techniques involving the creation of nano-holes in two dimensional (2D) MOs has facilitated the accessibility of active sites by exposing greater surface area,^{3–5} thus making these materials attractive for surface-sensitive applications in energy, sensing, and heterogeneous catalysis.^{6–8}

Further, the intrinsic polycrystallinity of these holey 2D structures can overcome the critical shortcoming of irreversible restacking of pristine 2D nanosheets.^{9,10} Recent advances in the synthesis of polycrystalline holey 2D MOs include the heterogeneous deposition of mixed transition metal oxides (TMOs) on graphene nanosheets as a sacrificial template¹¹ and the synthesis of holey TMOs by etching pristine 2D TMOs.^{12–14} Despite considerable improvements in the performances of these nanostructures, challenges, such as complex synthesis

^aSchool of Materials Science and Engineering, UNSW Sydney, Sydney, NSW 2052, Australia. E-mail: s.seifimofarah@unsw.edu.au, c.sorrell@unsw.edu.au

^bDepartament de Física, Universitat Politècnica de Catalunya, Campus Nord B4-B5, E-08034 Barcelona, Spain

^cResearch Centre for Functional Materials (RCFM), National Institute for Materials Science (NIMS), Tsukuba, Ibaraki 305-0047, Japan

^dAdvanced Electron Microscopy Division, Institute of Materials Science, Technische Universität Darmstadt, Alarich-Weiss-Strasse 2, 64287 Darmstadt, Germany

^eParticles and Catalysis Research Group, School of Chemical Engineering, UNSW Sydney, Sydney, NSW 2052, Australia

^fElectron Microscopy Unit (EMU), Mark Wainwright Analytical Centre, UNSW Sydney, Sydney, NSW 2052, Australia

^gSchool of Chemical Engineering, UNSW Sydney, NSW 2052, Australia

^hSchool of Chemistry, UNSW Sydney, Sydney, NSW 2052, Australia

ⁱCentre for Advanced Materials & Industrial Chemistry (CAMIC), School of Science, RMIT University, 124 La Trobe Street, Melbourne VIC 3000, Australia

^jLaboratory of Advanced Catalysis for Sustainability, School of Chemistry, University of Sydney, NSW 2006, Australia

^kSchool of Engineering, Western Sydney University, Penrith, NSW 2751, Australia

^lInternational Centre for Materials Nanoarchitectonics (MANA), National Institute for Materials Science (NIMS), 1-1 Namiki, Tsukuba, Ibaraki 305-0044, Japan

† Electronic supplementary information (ESI) available. See DOI: 10.1039/d0nr08097g

procedures, use of surfactants and templates, excessive nanosheet thicknesses, and low yields, limit their practical applicability.¹⁵ Unlike TMOs, there are few reports of pristine 2D rare earth oxides (REOs), none of which exhibit intrinsically layered structures. Consequently, complex methods of self-assembly have been applied as an alternative.^{16,17} Although such nanostructures have shown outstanding catalytic and photocatalytic performance,¹⁸ they have the disadvantage of low-yield production.¹⁹

The present work reports a novel strategy to synthesis free-standing, macroporous, polycrystalline 3D structures consisting of ultrathin 2D holey nanosheets of CeO_{2-x} . The fabrication process involves restacking of a newly developed cerium-based coordination polymer (Ce-CP) present in the form of nanosheets followed by burst exfoliation to achieve a hybrid 2D–3D CeO_{2-x} showed high densities of accessible active sites owing to having surface areas and pore volume as high as $251 \text{ m}^2 \text{ g}^{-1}$ and $1.15 \text{ cm}^3 \text{ g}^{-1}$, respectively, that yields a superior CO conversion performance ($T_{90\%} = 148 \text{ }^\circ\text{C}$) compared to all the pristine CeO_2 reported to date. The hybrid 2D–3D CeO_{2-x} can further be used as a template for decoration of a wide range of oxides including MnO , CuO , AgO , and RuO_2 to form a hetero-junction nanostructure, while maintain the original 2D–3D architecture. The catalytic performance of the CuO-CeO_{2-x} heterostructure exhibited a considerable improvement ($T_{90\%} = 88 \text{ }^\circ\text{C}$), which is interpreted in terms of the active sites associated with the TMOs identified through structural analyses and density functional theory (DFT) simulations.

Results and discussion

Fabrication of porous CeO_2 nanotubes derived from cerium-based coordination polymer

In order to synthesize the 2D–3D CeO_{2-x} , we used a novel cerium-based coordination polymer (Ce-CP) as the sole precursor, which was fabricated electrochemically at room temperature.⁹ This resulted in the formation of free-standing hexagonal tubes grown vertically on fluorine-doped tin oxide (FTO) substrates. The Ce-CP has the molecular formula of $\text{Ce}(\text{TCA})_2(\text{OH})_2 \cdot 2\text{H}_2\text{O}$ (TCA–trichloroacetate) and the β -axis view of the structure is shown schematically in Fig. 1a, where the unit cell with triclinic structure (space group $P\bar{1}$) is also defined.

The Ce ions are covalently bonded to the O^{2-} ions of H_2O , OH^- , and TCA, thereby forming stacked layers of thickness 1.04 nm (α -spacing). However, the terminating Cl^- ions of TCA at opposite interfaces are electrostatically attracted to protons, as evidenced from zeta potential (ξ) measurements (Fig. S1†). It is significant that the Ce-CP can be transformed into CeO_2 , shown in Fig. 1b, through simple oxidation. This transformation is shown schematically in Fig. 1c, where a dense distribution of nanopores results from TCA removal, shrinkage, and formation of a porous CeO_2 nanotube (Ce-NT); the successful synthesis of the Ce-NT is shown by scanning electron microscopy (SEM) imaging (Fig. 1d–f).

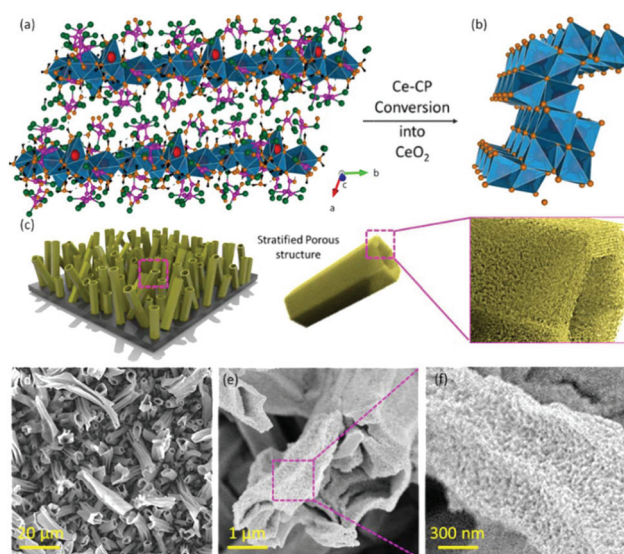


Fig. 1 (a) Schematic of β -axis projection of Ce-CP molecule; (b) schematic of CeO_2 molecule; (c) schematic of porous CeO_2 nanotubes on FTO substrate oxidized at $450 \text{ }^\circ\text{C}$ in air; (d–f) SEM images of porous CeO_2 nanotubes.

Fabrication of 2D–3D CeO_{2-x} Scaffold through exfoliation of Ce-CP

The simple exfoliation and rapid oxidation of the Ce-CP provide the means of tailoring the resultant CeO_2 architectures. The formation of 2D–3D oxides involves a two-step process of exfoliation of the bulk-layered Ce-CP in polar triethanolamine (TEA), followed by the transfer of the suspension to a furnace and heat treatment at $450 \text{ }^\circ\text{C}$ in air, as shown in Fig. 2a. The exfoliation results in a stable colloidal system ($\xi = +34 \text{ V}$) of individual Ce-CP monolayers (Fig. S1†). The heating process leads to conversion of the Ce-CP layers into CeO_{2-x} through evaporation of the interlayer-trapped TEA, resulting in a mesoporous 3D structure.

The importance of the kinetics in the engineering of the final nanostructures (Fig. S2†) is shown by the effects of the heating rate. Fig. 2b and c show that a slow heating rate ($0.2 \text{ }^\circ\text{C min}^{-1}$) allowed the laminar evaporation of TEA, resulting in a stacked solid macrolayer of CeO_{2-x} covered by intact hemispheres (Fig. S2a†). An intermediate heating rate ($1.0 \text{ }^\circ\text{C min}^{-1}$) caused fracture of the hemispheres owing to gas exudation; however, the hemispherical shapes were retained (Fig. S2b and c†). In contrast, fast heating rates ($3.0 \text{ }^\circ\text{C min}^{-1}$ and $6.0 \text{ }^\circ\text{C min}^{-1}$) caused energetic volumetric evaporation of TEA, nanostructural disruption, and formation of thick mesoporous macrolayers (Fig. 2d and e). The significance of TEA in exfoliation is highlighted by contrasting with the conventional oxidation of metal-based coordination polymers (MCPs), where the original microstructure is retained.^{20–22}

Further, high-magnification SEM images, as shown in Fig. 3a–c, reveal nanostructures consisting of clustered 2D nanosheets in 3D spherical morphology. High resolution transmission electron microscopy (HRTEM) image and the

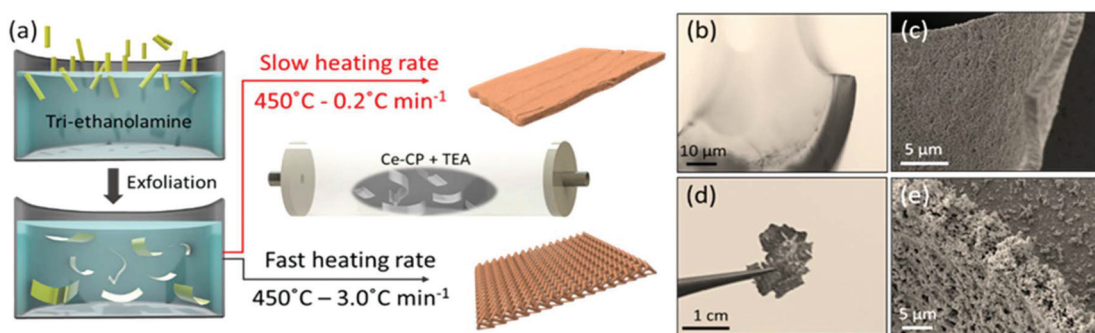


Fig. 2 (a) Schematic of two-step process of Ce-CP nanotube exfoliation in stirred TEA solution and oxidation at 450 °C in air into stacked CeO_{2-x} macrolayers; (b–e) CeO_{2-x} morphologies derived from Ce-CP.

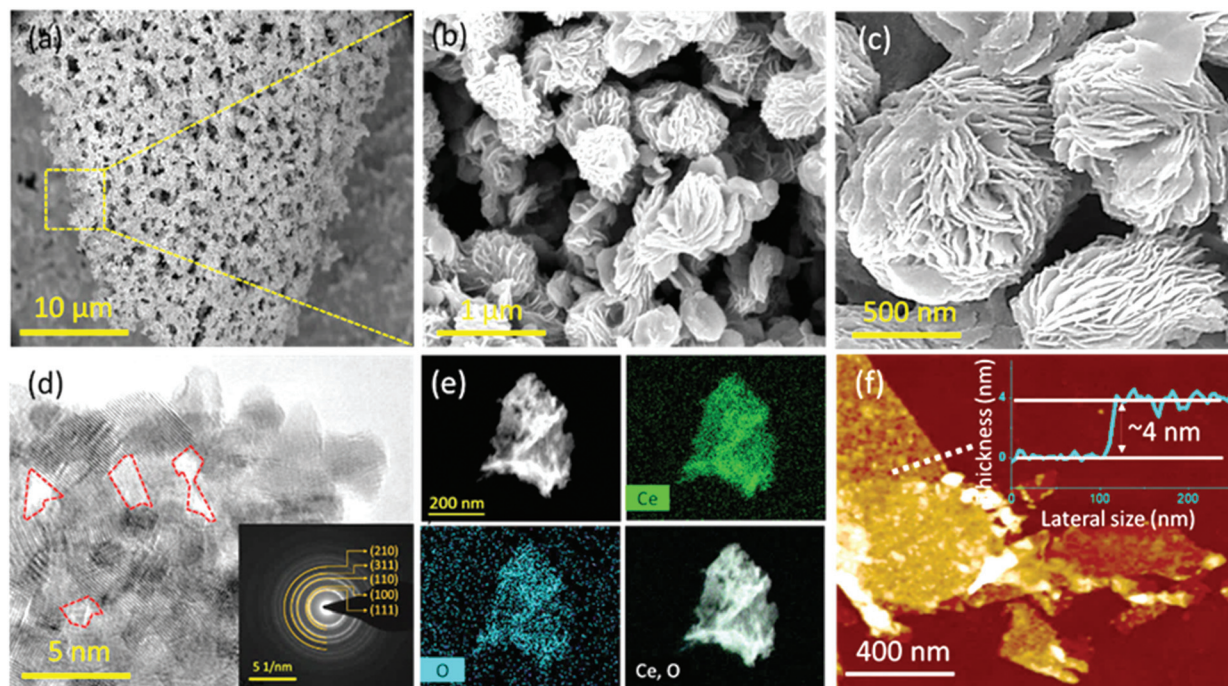


Fig. 3 (a–c) SEM images of hybrid 2D–3D CeO_{2-x}; (d) HRTEM image and SAED of holey 2D CeO_{2-x} nanosheet (holes outlined); (e) EDS elemental mapping of holey 2D CeO_{2-x} nanosheet; (f) AFM image (step height in white dotted line) and corresponding height profile of holey 2D CeO_{2-x} nanosheet.

selected area diffraction (SAED) pattern (Fig. 3d) of an individual nanosheet show that the holey CeO_{2-x} architecture is comprised of polycrystalline CeO₂ (space group of Fm3 m) with an extensive nanohole network of the nanosheet. Further, Fig. 3d illustrates the polycrystalline nature of the nanosheets, consisting of crystallite of 4–6 nm size and high concentrations of pores of 4–7 nm size. Energy dispersive X-ray spectroscopy (EDS) elemental mapping of the holey nanosheet (Fig. 3e) illustrates homogenous distributions of cerium and oxygen. Atomic force microscopy (AFM) imaging (Fig. 3f) shows an example of a nanosheet with a thickness of ~4 nm, which represents ~8 unit cells of cubic CeO₂, although the average thickness of the sheets was ~20–30 nm, which still represents remarkably thin holey nanosheets.

The wide-ranging applicability of the fabrication process is demonstrated by the one-step synthesis of various heterogeneous nanostructures through the addition of water-soluble transition metal salts (CuNO₃ or Mn(NO₃)₂) during the Ce-CP exfoliation step. Subsequent heat treatment and oxidation resulted in the formation of 2D–3D CeO_{2-x} decorated homogeneously with CuO (Ce–Cu) or MnO (Ce–Mn) of unchanged morphologies, in common with the pristine 2D–3D CeO_{2-x} nanostructures. It is worth noting that such a newly established process, involving the use of Ce-CP, can be applied to wider range of oxides such as MoO₃ and RuO₂. The detailed characterisation of the heterojunction MoO₃–CeO_{2-x} (Mo–Ce) and RuO₂–CeO_{2-x} (Ru–Ce) including SEM, TEM, and EDS are shown in Fig. S3–6.†

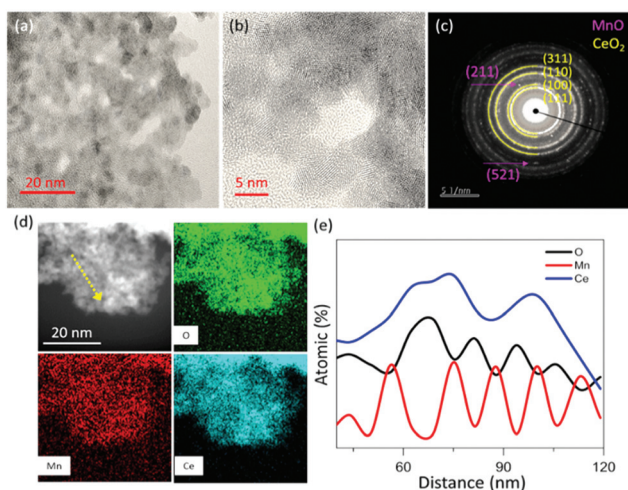


Fig. 4 Characterisation of holey Mn–Ce nanosheet (a) TEM; (b) HRTEM; (c) SAED pattern; (d) STEM elemental mapping and (e) line scan of O, Mn, Ce.

This is confirmed by HRTEM imaging of the Ce–Mn, as shown in Fig. 4a and b. The corresponding SAED pattern for the Ce–Mn, shown in Fig. 4c, reveals two sets of spots, associated with the cubic crystal structure of MnO, between the rings indicative of polycrystalline CeO₂ nanosheets. Further, Fig. 4d illustrates HRTEM imaging and corresponding scanning tunneling electron microscopy (STEM) images of the Ce–Mn, where Mn is homogeneously distributed across a CeO₂ nanosheet.

The concentration variations of the principal elements in the Ce–Mn were investigated using line scanning in the area highlighted by the yellow dotted arrow in Fig. 4d. The resultant line profiles, shown in Fig. 4e, reveal a number of features. First, the relatively consistent Mn peak distribution indicates essentially regular surface coverage by MnO. Second, the relatively consist-

ent Mn peak height and the irregular Ce peak pattern indicate that selective detection of the cation Mn over that of the cation Ce of the CeO_{2-x} background nanosheet. Third, the deep troughs in the Ce scan are indicative of the presence of holes. Fourth, the continued consistent presence of Mn at the hole locations suggests that MnO decorates the inner diameters of the holes. Fifth, the unexpected trend between Mn and O (stoichiometry 1/1), which would be expected to trend identically, was reversed owing to selective detection of the anion O in the CeO_{2-x} background nanosheet (stoichiometry 1/2), where the oxygen gradient is a compromise between the two cation gradients. The representative structural, microstructural, chemical, and morphological characteristics of Cu–Ce and Mn–Ce are provided in Fig. S7–S14.†

Defect analysis of 2D–3D CeO_{2-x} and mixed transition metal oxide heterojunction nanostructures

Fig. 5 illustrates the results for structural, defect, and surface analyses of the nanostructures. As shown in Fig. 5a, the quantitative analysis of Ce³⁺ concentration ([Ce³⁺]) of the mesoporous 2D–3D CeO_{2-x} can be studied using electron energy loss spectroscopy (EELS) data. Applying the linear relationship between the M₅/M₄ peak intensity ratio and the [V_O^{••}]^{23,24} a value of 12.8 at% was obtained for the latter, which shows higher Ce³⁺ concentration ([Ce³⁺]) than that of determined by X-ray photoelectron spectroscopy (XPS) (shown in Fig. S15†), which is 17 at% ([V_O^{••}] = 8.5 at%).²⁵

The laser Raman micro-spectroscopy spectra in Fig. 5b reveal the F_{2g} vibrational mode of Ce–O at ~464 cm⁻¹, confirming the presence of CeO₂.²⁶ The spectra for Cu–Ce and Mn–Ce reveal asymmetrical peak broadening of the F_{2g} peak at ~464 cm⁻¹ owing to quantum confinement effects.^{26,27} There also are two additional peaks at ~580 cm⁻¹ and ~1147 cm⁻¹ for all three

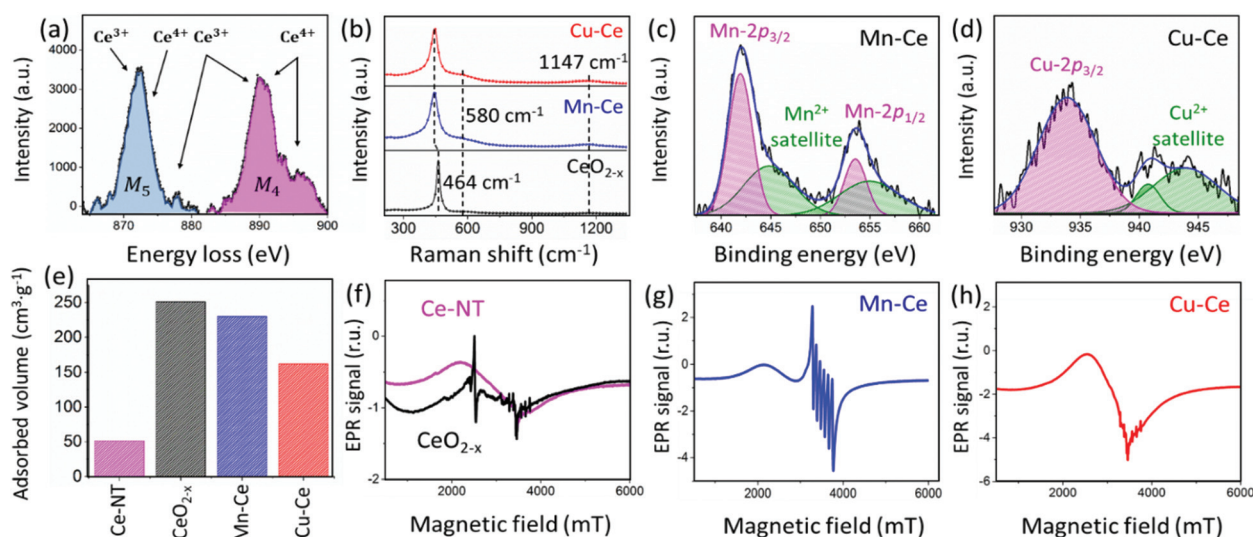


Fig. 5 Characterization of nanostructures: (a) EELS spectrum of 2D–3D CeO_{2-x}; (b) laser Raman microspectra 2D–3D CeO_{2-x}, Mn–Ce, Cu–Ce⁴⁶; (c) XPS Mn 2p spectrum of Mn–Ce. (d) XPS Cu 2p spectrum of Cu–Ce; (e) SSAs of Ce–NT, 2D–3D CeO_{2-x}, Mn–Ce, Cu–Ce; (f–h) EPR spectra of Ce–NT, 2D–3D CeO_{2-x}⁴⁶, Mn–Ce, Cu–Ce.

materials, which are attributed to the defect-induced mode (D) and 2nd order longitudinal optical mode (2LO), respectively, associated with V_{O}^{\bullet} .^{26,28,29} The use of Raman micro-spectroscopy as a powerful defect characterization tool has been studied in a review paper published by Yuwen *et al.*, in which the Raman spectra shown in Fig. 5b has been illustrated in Fig. S8† of corresponding Supporting Information.⁴⁶ The XPS data for the TMO-decorated CeO_{2-x} in Fig. 5c and d reveal shoulder peaks (green), which are indicative of Mn^{2+} and Cu^{2+} satellites, supporting the presence of MnO (which is confirmed by SEM, TEM, STEM, and EDS data shown in Fig. S8–11†) and CuO (as shown in the SEM, TEM, and EDS data of Fig. S12–S14†).^{30,31}

The Brunauer–Emmett–Teller (BET) specific surface areas (SSA) were determined to be 51, 251, 230, and 160 $\text{m}^2 \text{g}^{-1}$ for the Ce-NT, CeO_{2-x} , Mn–Ce, and Cu–Ce nanostructures, respectively, as shown in Fig. 5e. The sizes and volumes of the pores are also tabulated (Table S1†) and the corresponding plots are shown in Fig. S16.† The significant effect of exfoliation on increasing the SSA and the pore volume is shown by the respective fivefold and eightfold increases for the Ce-NT ($51 \text{ m}^2 \text{g}^{-1}$ – $0.14 \text{ cm}^3 \text{g}^{-1}$) and the 2D–3D CeO_{2-x} ($251 \text{ m}^2 \text{g}^{-1}$ – $1.15 \text{ cm}^3 \text{g}^{-1}$). The higher SSA for Mn–Ce relative to that of Cu–Ce is attributed to the formation of a compact laminated nanostructure (Fig. S12†) for the latter compared to the clustered 2D nanosheets in 3D spherical morphology for the former (Fig. S8†).

Structural defects were probed by electron paramagnetic resonance (EPR) analyses, as shown in Fig. 5f–h. For the Ce-NT in Fig. 5f, the single hyperfine in Fig. S17† indicates only the Ce^{3+} – O – Ce^{4+} defect³² at a negligible concentration, as shown in Fig. S24†, Supporting Information, of the work previously reported by Mofarah *et al.*⁹ For the 2D–3D CeO_{2-x} in Fig. 5f, the hyperfines in Fig. S18† reveal the presence of Ce^{3+} , O_2^- , and Ce^{3+} – O – Ce^{4+} defects at higher concentrations. These relative concentrations were derived from the total peak areas (using the baselines) of the second integrals of the EPR signal. For the Mn–Ce and Cu–Ce in Fig. 5(g and h), the respective hyperfines in Fig. S19 and S20† reveal that the fabrication of the heterojunction nanostructures introduces new defects associated with TMOs at even higher concentrations than were detected for 2D–3D CeO_{2-x} . Further, the EPR results of the Ce-NT and the 2D–3D CeO_{2-x} (Fig. 5f) have been provided in Fig. S9d† of the work published by Yuwen *et al.*⁴⁶ to highlight the importance of EPR in defect analysis of oxide nanostructures.

The hyperfine interaction between electrons and nuclei provides information concerning the number and identity of ions and their distances from unpaired electrons. Mn and Cu are of valence 2+, with the former having one stable isotope (^{55}Mn) and the latter having two stable isotopes (^{63}Cu , ^{65}Cu). Since Mn and Cu have the respective electron configurations of $3d^2$ and $3d^3$, they exhibit four and six absorption signals, respectively, as shown in Fig. S19 and S20.† Ce has four stable isotopes (^{136}Ce , ^{138}Ce , ^{140}Ce , ^{142}Ce) and two valences, 3+ and 4+, with corresponding electron configurations of $4f^1$ and $5p^6$.

Although the filled d orbital could result in the presence of ten absorption peaks, Ce^{4+} has no unpaired electrons and accordingly is EPR-inactive, while Ce^{3+} has a single unpaired

electron (EPR-active). However, other EPR absorption peaks can be generated by other unpaired electrons resulting from V_{O}^{\bullet} , V_{O}^{\times} , O_2^- , and Ce^{3+} – O – Ce^{4+} .²⁹ Table S2† provides the g -factors corresponding to the observed hyperfines. The 2D–3D CeO_{2-x} , Cu–Ce, and Mn–Ce exhibit six hyperfine that correspond to values characteristic of the defect Ce^{3+} – O ,³² albeit with g -factors shifted to lower values relative to that of 2.00 for the free electron of Ce-NT. The shift is effectively the maximal that can be exhibited by the paramagnetic impurities Mn ($3d^2$) and Cu ($3d^3$), which have shells that are less than the half-full. Consequently, the shifted g -factors can be attributed to the Mn and Cu species, the EPR signals of which are manifested in the form of shoulders on the sharp peaks and rounded humps with the hyperfines.

The first integral of the hyperfines indicates the total number of electronic charge carriers and the second integral assesses the total concentration of all defects with unpaired electrons. Fig. S17–S20† assess these integrals for all of the nanostructures, revealing the defect and charge carrier concentrations, which are assumed to be electrons since CeO_{2-x} is an n-type semiconductor, although it may exhibit p-type semiconductivity under some peculiar conditions, owing to the known presence of cerium vacancies (V''''_{Ce}).⁹

The decrease in the first integral is owing to the effect of the energy levels of the trapped electrons, which is in turn reflected in the changes to the g -factors, that are effectively controlled by the band positions. The reason for the decrease in the double integral reflects the balance of the annihilation and creation of defects resulting from the introduction of the decorating TMOs for the heterojunctions.

Fig. 5b shows that the $[V_{\text{O}}^{\bullet}]$ for the TMO-decorated heterostructures were greater than that for the 2D–3D mesoporous CeO_{2-x} , which suggests that other defects were annihilated. These were likely surface structural defects that were blocked by the apposition of the TMO particles. This result is supported by the decrease in surface areas of the decorated heterostructures, as shown in Fig. 5f. Another source of defects is intervalence charge transfer (IVCT), which can both create and eliminate defect states.³³

CO-conversion catalysis and DFT simulation

Fig. 6a provides the catalytic performance by the nanostructures in terms of the temperatures for 10, 50, and 90% CO conversion ($T_{10\%}$, $T_{50\%}$, $T_{90\%}$). The $T_{10\%}$ value for the Ce-NT sample was 160 °C and the $T_{90\%}$ was 372 °C, which are consistent with previous reports for pristine micron-sized CeO_2 .^{34,35} In contrast, the 2D–3D CeO_{2-x} exhibited outstanding performance, with a $T_{90\%}$ of 148 °C, which is the lowest temperature among the best-performing pristine CeO_{2-x} nanostructures, as shown by the red line in Fig. 6b. It is worth mentioning that CeO_2 and CeO_2 -based nanostructures have been applied to the catalytic reaction involving many other gases, including CO_2 ,³⁶ CH_4 ,³⁷ NO_x ,^{38,39} and SO_x ⁴⁰ as well as electrocatalysis for HER and OER.^{41,42} Additionally, CeO_2 -based materials have shown great promise in ozonation,⁴³ selective NO reduction,⁴⁴ and ethanol reforming reactions.⁴⁵ In the present work, the long-term stability of the 2D–3D CeO_{2-x} catalyst was shown over a period of 10 h at a con-

lizes a newly developed Ce-based coordination polymer precursor of stratified structure that can be exfoliated rapidly. During subsequent heating, the stacked-layer precursor converts into different morphologies of 2D–3D CeO_{2-x}, depending on control of the kinetics of organic oxidation. The resultant nanostructures show ultra-high surface areas, defect densities, and pore volumes, which are responsible for unparalleled catalytic performance for CO conversion. The performance was improved even further by modifying the 2D–3D CeO_{2-x} via TMO decoration to form heterojunction nanostructures. The enhanced catalytic activities on using MnO or CuO, as the TMO modifier, were investigated systematically using structural analyses and first principles DFT simulations. This high-yield synthesis technique offers a promising direction for simplified, cost-effective, industrial-scale, and highly controllable processes to produce functional nanocatalysts.

Author contributions

S.S.M. designed the project, conducted most of the experiments, characterization, provided the first draft, and worked on all the corresponding revisions. L.S. and X.Z. synthesized heterojunction Mn–Ce and Cu–Ce nanostructures and assisted with TEM, SEM, and Raman. C.C. implemented the first-principles simulations, wrote the related section, and commented on the final version of the draft. E.A. performed EELS characterization and commented on the final version of the draft. C. T. and J.S. conducted the CO-conversion tests and provided catalytic results. R.S. conducted the EPR tests and provided the corresponding analysis. Y.Y. conducted AFM imaging. R.A. assisted with experimental design and revision of the drafts. Y. W. and H.A. assisted with analyzing the catalytic performance, commented, and worked on the final versions of the draft. L.S. assisted in setting up the electrochemical cell, conducting Ce-CP synthesis, and revision of the drafts. V.W. assisted with synthesis of the 2D–3D CeO₂ samples for stability and reusability catalytic tests. E.D. performed SSA test for Ce-NT and commented on the final version of the draft. P.K. contributed to the data analyses and revised final version of the manuscript. C.C. S. worked on all drafts of the manuscript and supervised the overall project.

Funding

This work has been supported by the Australian Research Council (DP170104130). The authors are grateful for access to the characterization facilities provided by the Mark Wainwright Analytical Centre, UNSW Sydney and beam time at the Wombat beamline of the Australian Nuclear Science and Technology Organization (ANSTO). S.S.M. is pleased to acknowledge UIPA and RTP scholarship support from UNSW Sydney. E.A. acknowledges the financial support (JSPS KAKENHI Grant Number: 18F18064) provided by the Japan Society for the Promotion of Science.

Conflicts of interest

The authors declare no competing financial interest.

Acknowledgements

We acknowledge the Mark Wainwright Analytical Centre, Sydney, Australia for provision of subsidised use of characterisation facilities and assisting with data analysis. Further, we acknowledge Setareh M. Pour for providing the schematic images in this work.

Notes and references

- 1 Q. Zhang, I. Lee, J. Ge, F. Zaera and Y. Yin, *Adv. Funct. Mater.*, 2010, **20**(14), 2201–2214.
- 2 E. Doustkhah and Y. Ide, *ACS Appl. Nano Mater.*, 2019, **2**(12), 7513–7520.
- 3 K. Shen, L. Zhang, X. Chen, L. Liu, D. Zhang, Y. Han, J. Chen, J. Long, R. Luque, Y. Li and B. Chen, *Science*, 2018, **359**(6372), 206–210.
- 4 K. Lan, Y. Liu, W. Zhang, Y. Liu, A. Elzatahry, R. Wang, Y. Xia, D. Al-Dhayan, N. Zheng and D. Zhao, *J. Am. Chem. Soc.*, 2018, **140**(11), 4135–4143.
- 5 L. Peng, Z. Fang, J. Li, L. Wang, A. M. Bruck, Y. Zhu, Y. Zhang, K. J. Takeuchi, A. C. Marschilok, E. A. Stach, E. S. Takeuchi and G. Yu, *ACS Nano*, 2018, **12**(1), 820–828.
- 6 J. Xiong, J. Di, J. Xia, W. Zhu and H. Li, *Adv. Funct. Mater.*, 2018, **28**, 39.
- 7 D. Voiry, H. S. Shin, K. P. Loh and M. Chhowalla, *Nat. Rev. Chem.*, 2018, **2**, 0105.
- 8 K. Kalantar-Zadeh, Z. O. Jian, T. Daeneke, A. Mitchell, T. Sasaki and M. S. Fuhrer, *Appl. Mater. Today*, 2016, **5**, 73–89.
- 9 S. S. Mofarah, E. Adabifiroozjaei, R. Pardehkorram, M. H. N. Assadi, M. Hinterstein, Y. Yao, X. Liu, M. B. Ghasemian, K. Kalantar-Zadeh, R. Mehmood, C. Cazorla, R. Shahmiri, G. Bahmanrokh, S. Bhattacharyya, M. C. Spadaro, J. Arbiol, S. Lim, Y. Xu, H. Arandiyani, J. Scott, P. Koshy and C. C. Sorrell, *Adv. Mater.*, 2019, **31**(52), 1905288.
- 10 L. Peng, Z. Fang, Y. Zhu, C. Yan and G. Yu, *Nat. Energy*, 2018, **8**(9), 1702179.
- 11 L. Peng, P. Xiong, L. Ma, Y. Yuan, Y. Zhu, D. Chen, X. Luo, J. Lu, K. Amine and G. Yu, *Nat. Commun.*, 2017, **8**, 15139.
- 12 W. Wen, J. M. Wu and M. H. Cao, *Nanoscale*, 2014, **6**(21), 12476–12481.
- 13 G. Zhang, L. Ren, Z. Yan, L. Kang, Z. Lei, H. Xu, F. Shi and Z. H. Liu, *Chem. Commun.*, 2017, **53**(20), 2950–2953.
- 14 X. Bo, Y. Li, R. K. Hocking and C. Zhao, *ACS Appl. Mater. Interfaces*, 2017, **9**(47), 41239–41245.
- 15 Z. Fang, L. Peng, Y. Qian, X. Zhang, Y. Xie, J. J. Cha and G. Yu, *J. Am. Chem. Soc.*, 2018, **140**(15), 5241–5247.

- 16 Y. Sun, Q. Liu, S. Gao, H. Cheng, F. Lei, Z. Sun, Y. Jiang, H. Su, S. Wei and Y. Xie, *Nat. Commun.*, 2013, **4**, 2899.
- 17 T. Yu, B. Lim and Y. Xia, *Angew. Chem., Int. Ed.*, 2010, **49**(26), 4484–4487.
- 18 S. S. Mofarah, E. Adabifiroozjaei, Y. Wang, H. Arandiyan, R. Pardehkhorrām, Y. Yao, M. H. N. Assadi, R. Mehmood, W.-F. Chen, C. Tsounis, J. Scott, S. Lim, R. Webster, V. Zhong, Y. Xu, P. Koshy and C. C. Sorrell, *J. Mater. Chem. A*, 2020, **8**, 4753–4763.
- 19 Z. Zhu, H. Yin, C. T. He, M. Al-Mamun, P. Liu, L. Jiang, Y. Zhao, Y. Wang, H. G. Yang, Z. Tang, D. Wang, X. M. Chen and H. Zhao, *Adv. Mater.*, 2018, **30**(28), 1801171.
- 20 F. Zou, X. Hu, Z. Li, L. Qie, C. Hu, R. Zeng, Y. Jiang and Y. Huang, *Adv. Mater.*, 2014, **26**(38), 6622–6628.
- 21 R. R. Salunkhe, J. Tang, Y. Kamachi, T. Nakato, J. H. Kim and Y. Yamauchi, *ACS Nano*, 2015, **9**(6), 6288–6296.
- 22 F. Zhang, C. Chen, W.-m. Xiao, L. Xu and N. Zhang, *Catal. Commun.*, 2012, **26**, 25–29.
- 23 B. Feng, I. Sugiyama, H. Hojo, H. Ohta, N. Shibata and Y. Ikuhara, *Sci. Rep.*, 2016, **6**, 20288.
- 24 S. S. Mofarah, E. Adabifiroozjaei, Y. Yao, P. Koshy, S. Lim, R. Webster, X. Liu, R. Khayyam Nekouei, C. Cazorla, Z. Liu, Y. Wang, N. Lambropoulos and C. C. Sorrell, *Nat. Commun.*, 2019, **10**, 2594.
- 25 R. Mehmood, X. Wang, P. Koshy, J. L. Yang and C. C. Sorrell, *CrystEngComm*, 2018, **20**(11), 1536–1545.
- 26 Z. Wu, M. Li, J. Howe, H. M. Meyer and S. H. Overbury, *Langmuir*, 2010, **26**(21), 16595–16606.
- 27 I. Kosacki, T. Suzuki, H. U. Anderson and P. Colomban, *Solid State Ion.*, 2002, **149**, 99–105.
- 28 J. E. Spanier, R. D. Robinson, F. Zhang, S.-W. Chan and I. P. Herman, *Phys. Rev. B: Condens. Matter Mater. Phys.*, 2001, **64**(24), 2454071–2454078.
- 29 J. M. López, A. L. Gilbank, T. García, B. Solsona, S. Agouram and L. Torrente-Murciano, *Appl. Catal., B*, 2015, **174–175**, 403–412.
- 30 E. S. Ilton, J. E. Post, P. J. Heaney, F. T. Ling and S. N. Kerisit, *Appl. Surf. Sci.*, 2016, **366**, 475–485.
- 31 Q. Zhang, L. Huang, S. Kang, C. Yin, Z. Ma, L. Cui and Y. Wang, *RSC Adv.*, 2017, **7**(69), 43642–43647.
- 32 L. Wang, Y. Yu, H. He, Y. Zhang, X. Qin and B. Wang, *Sci. Rep.*, 2017, **7**, 12845.
- 33 W. F. Chen, S. S. Mofarah, D. A. H. Hanaor, P. Koshy, H. K. Chen, Y. Jiang and C. C. Sorrell, *Inorg. Chem.*, 2018, **57**(12), 7279–7289.
- 34 X. Zhou, J. Ling, W. Sun and Z. Shen, *J. Mater. Chem. A*, 2017, **5**(20), 9717–9722.
- 35 K. Kim, J. D. Yoo, S. Lee, M. Bae, J. Bae, W. Jung and J. W. Han, *ACS Appl. Mater. Interfaces*, 2017, **9**(18), 15449–15458.
- 36 K. Chang, H. Zhang, M.-J. Cheng and Q. Lu, *ACS Catal.*, 2020, **10**(1), 613–631.
- 37 E. C. Lovell, J. Horlyck, J. Scott and R. Amal, *Appl. Catal., A*, 2017, **546**, 45–47.
- 38 H. Chang, J. Li, J. Yuan, L. Chen, Y. Dai, H. Arandiyan, J. Xu and J. Hao, *Catal. Today*, 2013, **201**, 139–144.
- 39 C. Liu, L. Chen, H. Chang, L. Ma, Y. Peng, H. Arandiyan and J. Li, *Catal. Commun.*, 2013, **40**, 145–148.
- 40 A. Rodas-Grapaín, J. Arenas-Alatorre, A. Gómez-Cortés and G. Díaz, *Catal. Today*, 2005, **107–108**, 168–174.
- 41 Z. Zheng, N. Li, C. Q. Wang, D. Y. Li, Y. M. Zhu and G. Wu, *Int. J. Hydrogen Energy*, 2012, **37**, 13921–13932.
- 42 S. M. Yang, S. Lee, J. Jian, W. Zhang, P. Lu, Q. Jia, H. Wang, T. W. Noh, S. V. Kalinin and J. L. MacManus-Driscoll, *Nat. Commun.*, 2015, **6**, 8588.
- 43 A. A. Esmailpour, S. Moradi, J. Yun, J. Scott and R. Amal, *Catal.: Sci. Technol.*, 2019, **9**, 5979–5990.
- 44 C. Liu, L. Chen, J. Li, L. Ma, H. Arandiyan, Y. Du, J. Xu and J. Hao, *Environ. Sci. Technol.*, 2012, **46**(11), 6182–6189.
- 45 Z. Niazi, A. Irankhah, Y. Wang and H. Arandiyan, *Int. J. Hydrogen Energy*, 2020, **45**, 21512–21522.
- 46 Y. Xu, S. S. Mofarah, R. Mehmood, C. Cazorla, P. Koshy, and C. C. Sorrell, *Mater. Horiz.*, 2021, **8**(1), 102–123.
- 47 S. S. Mofarah, R. Khayyam Nekouei, S. Maroufi, S. Biswal, S. Lim, Y. Yao and V. Sahajwalla, *Nanoscale*, 2021, **13**, 3662–3672.